

H I, CO, and *Planck*/*IRAS* dust properties in the high-latitude-cloud complex, MBM 53, 54, 55 and HLCG 92–35; Possible evidence for an optically thick H I envelope around the CO clouds

Yasuo Fukui¹, Ryuji Okamoto¹, Ryohei Kaji¹, Hiroaki Yamamoto¹, Kazufumi Torii¹,
Takahiro Hayakawa¹, Kengo Tachihara¹, John M. Dickey², Takeshi Okuda^{1,3},
Akio Ohama¹, Yutaka Kuroda¹, and Toshihisa Kuwahara¹

fukui@a.phys.nagoya-u.ac.jp

ABSTRACT

We present an analysis of the H I and CO gas in conjunction with the *Planck*/*IRAS* sub-mm/far-infrared dust properties toward the most outstanding high latitude clouds MBM 53, 54, 55 and HLCG 92–35 at $b = -30^\circ$ to -45° . The CO emission, dust opacity at 353 GHz (τ_{353}), and dust temperature (T_d) show generally good spatial correspondence. On the other hand, the correspondence between the H I emission and the dust properties is less clear than in CO. The integrated H I intensity $W_{\text{H I}}$ and τ_{353} show a large scatter with a correlation coefficient of ~ 0.6 for a T_d range from 16 K to 22 K. We find however that $W_{\text{H I}}$ and τ_{353} show better correlation for smaller ranges of T_d every 0.5 K, generally with a correlation coefficient of 0.7–0.9. We set up a hypothesis that the H I gas associated with the highest $T_d \geq 21.5$ K is optically thin, whereas the H I emission is generally optically thick for T_d lower than 21.5 K. We have determined a relationship for the optically thin H I gas between atomic hydrogen column density and τ_{353} , $N_{\text{H I}} (\text{cm}^{-2}) = (1.5 \times 10^{26}) \cdot \tau_{353}$, under the assumption that the dust properties are uniform, and applied it to estimate $N_{\text{H I}}$ from τ_{353} for the whole cloud. $N_{\text{H I}}$ was then used to solve for T_s and $\tau_{\text{H I}}$ over the region. The result shows that the H I is dominated by optically thick gas having low spin temperature of 20 K–40 K and density of 40 cm^{-3} – 160 cm^{-3} . The H I envelope has a total mass of $\sim 1.2 \times 10^4 M_\odot$, an order of magnitude larger than that of

¹Department of Physics, Nagoya University, Chikusa-ku, Nagoya 464-8602, Japan

²University of Tasmania, School of Maths and Physics, Private Bag 37, Hobart, TAS 7001, Australia

³National Astronomical Observatory of Japan, 2-21-1 Osawa, Mitaka, Tokyo 181-8588, Japan

the CO clouds. The HI envelope properties derived by this method do not rule out a mixture of HI and H₂ in the dark gas, but we present indirect evidence that most of the gas mass is in the atomic state.

Subject headings: ISM: clouds — ISM: individual objects (MBM 53, 54, 55 and HLCG 92–35) — radio lines: ISM

1. Introduction

The neutral interstellar medium (ISM) consists of HI, H₂, and possibly “dark gas”, which is believed to be undetectable in line emission of HI or CO (Grenier et al. 2005; *Planck* Collaboration et al. 2011b). The HI emission at 21 cm wavelength and the CO emission at 2.6 mm offer tools to probe atomic and molecular hydrogen. The CO clouds have low kinetic temperature 10 K–100 K with density above 1000 cm^{−3} as derived by analyses of multi- J CO transitions (e.g. Castets et al. 1990). The CO intensity is converted into molecular column density by an X_{CO} factor, which is empirically determined by assuming dynamical equilibrium of the CO clouds, dust properties measured in extinction and/or far-infrared emission, and comparison with gamma rays created by proton-proton collisions via neutral pion decay (e.g., Blitz et al. 2007; Fukui & Kawamura 2010; Bolatto et al. 2013). On the other hand, the physical parameters of the HI gas have been rather ambiguous, mainly because the HI emission has a single observed quantity, intensity as a function of velocity, for two independent variables spin temperature T_s and HI optical depth τ_{HI} , not allowing us to determine each of these observationally. The HI consists of warm and cold components (for a review see Kalberla & Kerp 2009; Dickey & Lockman 1990). The mass of the HI gas having spin temperature higher than ~ 100 K is measurable at reasonably high accuracy under the optically thin approximation, while the cold component having spin temperature of 20 K–80 K is measured by comparing the absorption and emission HI profiles only where background continuum sources are available (Dickey et al. 2003; Heiles & Troland 2003). It is notable that some recent works on TeV gamma-ray supernova remnants show that the cold HI gas which is not detectable in CO at 1σ integrated intensity level of ~ 1 K km s^{−1} (Fukui et al. 2012) is responsible for the gamma-rays via collision between cosmic-ray protons and interstellar protons (Fukui et al. 2012; Fukui 2013; Fukuda et al. 2014). However, the observed sample of cold HI is limited and the cold HI still needs further effort to better constrain its physical properties.

Recent progress in measuring the infrared and sub-mm emission over the whole sky is remarkable. These observations are strongly motivated by the aim to precisely measure the cosmic microwave background (CMB) radiation and its polarization. In particular, the *Planck*

collaboration released the whole sky distribution of dust temperature T_d and dust opacity τ_{353} at 5 arcmin resolution which have been achieved through sensitive measurements of the dust emission above 100 GHz in the Galactic foreground. Five papers of the *Planck* collaboration presented comparisons between CO and dust emission (*Planck* Collaboration et al. 2011b,e,d,c,f). These studies derived basic physical relationships between the neutral gas and the dust emission and concluded that the dark gas (Grenier et al. 2005) occupies 15 % of the interstellar medium (ISM), where the HI emission was assumed to be optically thin. Similar studies on 21 cm HI emission include Lee et al. (2012) and *Planck* Collaboration et al. (2011a).

The high latitude molecular clouds MBM 53, 54, 55 and HLCG 92–35 are one of the largest cloud systems in the sky at Galactic latitude of -30° – -50° with only minor background components (Magnani et al. 1985). The distance of the cloud system is determined to be 150 pc (Welty et al. 1989). Yamamoto et al. (2003) used the NANTEN 4 m telescope to observe the $J=1-0$ transitions of ^{12}CO , ^{13}CO , and C^{18}O and mapped the molecular distribution. The velocity of the MBM 53, 54, 55 and HLCG 92–35 clouds is mainly in range from -11 km s^{-1} to 0 km s^{-1} for CO. The half-power beam widths were 2.6 arcmin–2.7 arcmin and their grid spacings are 4 or 8 arcmin for the ^{12}CO , 2 arcmin for the ^{13}CO and the C^{18}O . They also identified associated HI gas at 36 arcmin resolution and discussed that the HI gas is being converted into H_2 under the dynamical effect of a nearby shell driven by stellar winds. Gir et al. (1994) studied and identified the associated HI, while their coverage was limited to $\sim 1/2$ of the area studied by Yamamoto et al. (2003). For reference, this region is rich in high latitude clouds including a far-infrared looplike structure in Pegasus, and Yamamoto et al. (2006) observed this loop in CO($J=1-0$) lines. MBM 53, 54, 55 and HLCG 92–35 clouds show no sign of active star formation and are an ideal target to study detailed ISM properties under the general interstellar radiation field. The regions of the MBM 53, 54, 55 and HLCG 92–35 clouds and the Pegasus loop have also been used to test CO component separation in the analysis of the cosmic microwave background emission (Ichiki et al. 2014).

In order to better understand the detailed physical properties of the local ISM, we have undertaken new CO($J=1-0$) observations of MBM 53, 54, 55 and HLCG 92–35 in the on-the-fly mode with the 2.6 arcmin beam of the NANTEN2 4 m telescope as part of the NANTEN Super CO survey (=NASCO), which is aiming to cover 70 % of the sky. By using the HI dataset at 4 arcmin resolution from the GALFA archive data, we have compared the CO and HI with the *Planck/IRAS* dust properties. In this paper we present the first results from the detailed comparison. Section 2 describes the observations, Section 3 gives the results and analysis, and Section 4 presents conclusions. Another paper which deals with the dust emission covering the whole sky will be published separately (Fukui et al. 2014) and

is complementary to the present paper.

2. Observational datasets

In this study we used NANTEN2 CO data, GALFA HI data, the dust emission data measured by *Planck/IRAS*, and the 1.4 GHz radio continuum data. All the data are gridded to 1 arcmin, smaller than the angular resolutions of these datasets.

2.1. CO data

$^{12}\text{CO}(J=1-0)$ and $^{13}\text{CO}(J=1-0)$ emission were obtained by the NANTEN2 4 m millimeter/submillimeter telescope of Nagoya University, which is installed at an altitude of 4865 m in northern Chile. Observations of the $^{12}\text{CO}(J=1-0)$ and $^{13}\text{CO}(J=1-0)$ lines were simultaneously conducted in several sessions from 2011 November to 2013 January, and cover about 75 deg^2 . Only observational parameters of $^{12}\text{CO}(J=1-0)$ are described below. The front end was a 4 K cooled Nb Superconductor-Insulator-Superconductor (SIS) mixer receiver, and the double-sideband (DSB) system temperature was $\sim 200\text{ K}$ including the atmosphere toward the zenith. The spectrometer was a digital Fourier transform spectrometer (DFS) with 16,384 channels, providing velocity resolution of 0.2 km s^{-1} . All observations were conducted by using an on-the-fly (OTF) mapping technique with a 2.6 arcmin main beam at a 1 arcmin data sampling, and each spatial area of 1 degree by 1 degree was mapped several times in different scanning directions to reduce scanning effects by basket-weave technique (Emerson & Graeve 1988). These OTF data were reduced into FITS data cubes with the original IDL software. The rms noise fluctuations in $^{12}\text{CO}(J=1-0)$ spectra after basket-weave technique were $\sim 1.2\text{ K}$ per channel in the main beam temperature, T_{mb} . The CO data is smoothed to 5 arcmin spatial resolution to be compared with HI and *Planck/IRAS* datasets. The final rms noise fluctuations are $\sim 0.6\text{ K}$ per channel in a 5 arcmin smoothed beam. The pointing was checked regularly using planets, and the applied corrections were always smaller than 20 arcsec. The standard sources M17 SW and Ori KL were observed for intensity calibration. The CO intensity is integrated over a velocity range from -12 km s^{-1} to $+2\text{ km s}^{-1}$.

2.2. HI data

Archival datasets of the GALFA-HI survey are used (Peek et al. 2011). The survey was conducted on the Arecibo Observatory 305 m telescope and the angular resolution of the data is 4 arcmin. The rms noise fluctuations of the HI data are ~ 0.25 K per channel in T_{mb} . The HI data are also smoothed to 5 arcmin resolution, and the rms noise fluctuations of the final HI spectra are 0.2 K per channel for the 5 arcmin beam. The HI intensity is spread over a velocity range from -49 km s^{-1} to $+17 \text{ km s}^{-1}$, while most of the HI emission is between -25 km s^{-1} and $+12 \text{ km s}^{-1}$.

2.3. *Planck*/*IRAS* data

Archival datasets of the optical depth at 353 GHz (τ_{353}) and dust temperature (T_{d}) were obtained by fitting 353, 545, and 857 GHz data of the first 15 months observed by the *Planck* satellite and 100 micron data measured by the *IRAS* satellite. Both of these data have angular resolutions of 5 arcmin. For details, see the *Planck* Legacy Archive (PLA) explanatory supplement (*Planck* Collaboration 2013).

2.4. Radio continuum data

As the 1.4 GHz radio continuum background we use the CHIPASS data (Calabretta et al. 2014) for the region at $\delta(\text{J2000}) < 25^\circ$ and the data described in Reich (1982) and Reich & Reich (1986) for the region at $\delta(\text{J2000}) \geq 25^\circ$. Their spatial resolutions are 14.4 arcmin and 35 arcmin, respectively. Although these data have lower angular resolutions than the rest analyzed in the study, the peak radiation temperature of the continuum data shows small variations from ~ 3.4 K to ~ 4.9 K except for the area within ~ 30 arcmin of the quasar 3C 454.3, which happens to be located near the CO clouds (e.g., Abdo et al. 2011). We used these lower resolution data by excluding the area around 3C 454.3.

2.5. Masking

In the present analysis, the local interstellar medium toward the cloud system is approximated by a single layer. This is consistent with the velocity of the HI being peaked at around 0 km s^{-1} , and generally a single velocity component is dominant. In order to eliminate possible sources of contamination, we further applied the following masking. These

masked areas are listed in Table 1 (see also Figure 7).

- (1) The areas showing CO emission higher than 1.1 K km s^{-1} (1σ) are masked in order to exclude the contribution of the CO-emitting molecular gas.
- (2) The two regions where there is a secondary HI peak outside the velocity range from -25 km s^{-1} to $+12 \text{ km s}^{-1}$ are masked at $(\ell, b) \sim (81^\circ.5, -33^\circ.0)$, $(85^\circ.6, -33^\circ.8)$. Generally, these secondary peaks show intensity comparable to that of the main HI peak.
- (3) Regions with high T_d indicating localized heating by stars etc. are masked by referring to the *IRAS* point source catalog etc. The most extended region of such high T_d is located toward 3C 454.3, although the origin of the high T_d is not known.
- (4) The six regions where the HI data are missing are masked.

3. Results

Figure 1 shows four panels which present CO, HI and *Planck/IRAS* dust properties. Figure 1(a) shows the CO($J=1-0$) velocity integrated intensity distribution, W_{CO} (K km s^{-1}). Figure 1(b) shows an overlay of HI and CO where we confirm the associated HI in the previous works (Gir et al. 1994; Yamamoto et al. 2003). W_{HI} (K km s^{-1}) is the intensity of HI integrated from -49 km s^{-1} to $+17 \text{ km s}^{-1}$. Figure 1(c) presents an overlay of τ_{353} and CO. The comparison shows good correspondence between them within the CO contours, whereas the correspondence of HI with τ_{353} seems less clear than in the case of CO. We note that τ_{353} is significantly extended beyond the lowest CO contour 3.4 K km s^{-1} (3σ). Figure 1(d) shows an overlay of T_d and CO. The lowest $T_d \sim 16 \text{ K}$ is clearly associated with CO, and T_d increases up to $\sim 22 \text{ K}$ outside the CO clouds.

Figure 2(a) where masking in Section 2.5. is applied shows an average HI spectrum over the region in Figure 1, and Figure 2(b), the HI integrated intensity over the same longitude range, where $^{12}\text{CO}(J=1-0)$ intensity is superposed by black contours. Figure 2(a) indicates that most of the HI emission is in the range from -25 km s^{-1} to $+12 \text{ km s}^{-1}$ which is determined by the 10% level of the average HI spectrum and the HI emission from -25 km s^{-1} to $+12 \text{ km s}^{-1}$ has a single component, which includes 89% of the HI integrated intensity. The remaining 11% of the HI emission is mainly on the negative velocity side at $V_{\text{LSR}} < -25 \text{ km s}^{-1}$. In order to eliminate possible contamination of the HI at $V_{\text{LSR}} < -25 \text{ km s}^{-1}$ we shall adopt the HI velocity range from -25 km s^{-1} to $+12 \text{ km s}^{-1}$ in the following analysis and call this the main HI cloud. This velocity range includes the HI which

has been suggested to be associated with the CO clouds (Gir et al. 1994; Yamamoto et al. 2003), and more details are given in Appendix A on the HI velocity channel distributions (Figure 10).

In the following, τ_{353} and W_{HI} denote those quantities for the whole velocity range and $\tau_{353}(\text{main})$ and $W_{\text{HI}}(\text{main})$ for the main HI cloud only. The excluded velocity ranges from the main HI cloud have very weak HI intensity of $\lesssim 30 \text{ K km s}^{-1}$ (Figure 2(b)) and it is likely that this HI is optically thin. $W_{\text{HI}}(\text{main})$ is calculated from W_{HI} by subtracting the HI integrated intensity at $V_{\text{LSR}} < -25 \text{ km s}^{-1}$ and $V_{\text{LSR}} > +12 \text{ km s}^{-1}$. By adopting the relationship between τ_{353} and W_{HI} in the optically-thin limit (see below), $\tau_{353}(\text{main})$ is calculated from τ_{353} by subtracting a fraction of τ_{353} in proportion to $[W_{\text{HI}} - W_{\text{HI}}(\text{main})]/W_{\text{HI}}$, which corrects for the emission due to the velocity range excluded from HI main. The details of the subtraction are given in Appendix B.

Figures 3(a) and 4(a) show scatter plots between W_{HI} and τ_{353} for the main HI cloud and for the whole HI velocity span, respectively, in the region with masking (Section 2.5.). We note that Figures 3 and 4 show the same trend, as described below, indicating that the subtraction has a minor effect on the results as expected from the weakness of the subtracted HI intensity. The scattering is fairly large with correlation coefficients of ~ 0.6 in the both plots (Figures 3(a) and 4(a)). Since W_{HI} is supposed to be a good measure of the total HI in the optically thin approximation, τ_{353} should be highly correlated with W_{HI} with a high correlation coefficient, if the HI is optically thin, and if gas and dust are well mixed with uniform properties. The large scatter suggests that the dust properties may vary significantly, and/or that the optically thin approximation for the HI gas may not be valid.

In Figures 3(b), 3(c), 4(b), and 4(c), we indicate T_d for every 0.5 K interval at each point in Figures 3(a) and 4(a). We made least-squares fits between $W_{\text{HI}}(\text{main})$ and $\tau_{353}(\text{main})$ by linear regression for each T_d range. Since the number of data points becomes less for the highest T_d , the fitting accuracy becomes worse for higher T_d . In particular, for $T_d \geq 21.5 \text{ K}$ the number of points becomes much less than for the others, and we here assume that the intercept is zero and determine only the slope. The slopes k (K km s^{-1}), intercepts, and correlation coefficients are listed in Table 2. We note the correlation coefficient is around 0.7–0.9 for T_d higher than 18 K. This clearly shows that the correlation strongly depends on T_d , and becomes better for the smaller T_d ranges; generally speaking the slope becomes steeper and the intercept smaller with increasing T_d .

Figure 5(a) shows a scatter plot of T_d and $\tau_{353}(\text{main})$, and clearly indicates a significant decrease of T_d with $\tau_{353}(\text{main})$. A similar result that the dust temperature increases with decreasing gas column density has recently been found by the *Planck* Collaboration (Planck Collaboration et al. 2014; *Planck* Collaboration et al. 2014). Figure 5(b) shows a

scatter plot of W_{CO} and $\tau_{353}(\text{main})$ in the area observed in CO. This shows positive correlation with a correlation coefficient of ~ 0.7 , while the dispersion is large. The solid line in (b) represents a relationship $\tau_{353}(\text{main}) = [(1.8 \pm 0.8) \times 10^{-6}] \cdot W_{\text{CO}} (\text{K km s}^{-1}) + [(8.4 \pm 5.0) \times 10^{-6}]$, which is the result of a least-squares fit to the data with $W_{\text{CO}} \geq 3\sigma$.

4. Analysis

From the behavior in Figure 3 we infer that for the highest T_d the optically thin approximation of HI is valid, whereas for lower T_d the approximation becomes worse due to large HI optical depth. Equation (1) is used to estimate N_{HI} for the optically thin part in Figure 3,

$$N_{\text{HI}} (\text{cm}^{-2}) = (1.823 \times 10^{18}) \cdot W_{\text{HI}} (\text{K km s}^{-1}), \quad (1)$$

and the relationship between $\tau_{353}(\text{main})$ and $N_{\text{HI}}(\text{main})$ is estimated for the optically thin regime at $T_d \geq 21.5 \text{ K}$;

$$N_{\text{HI}}(\text{main}) (\text{cm}^{-2}) = (1.5 \times 10^{26}) \cdot \tau_{353}(\text{main}), \quad (2)$$

where 1.5×10^{26} is calculated by a product of 1.823×10^{18} in equation (1) and the slope k ($= 8.47 \times 10^7 \text{ K km s}^{-1}$) for $T_d > 21.5 \text{ K}$ in Table 2.

Relation (2) holds as long as the dust properties are uniform, allowing us to calculate $N_{\text{HI}}(\text{main})$ from $\tau_{353}(\text{main})$. Then the coupled equations (3) and (4) in the following are used to solve for T_s and $\tau_{\text{HI}}(\text{main})$, where $N_{\text{HI}}(\text{main})$ is calculated from $\tau_{353}(\text{main})$ by equation (2),

$$W_{\text{HI}}(\text{main}) (\text{K km s}^{-1}) = [T_s (\text{K}) - T_{\text{bg}} (\text{K})] \cdot \Delta V_{\text{HI}} (\text{km s}^{-1}) \cdot [1 - \exp(-\tau_{\text{HI}}(\text{main}))], \quad (3)$$

$$\tau_{\text{HI}}(\text{main}) = \frac{N_{\text{HI}}(\text{main}) (\text{cm}^{-2})}{1.823 \times 10^{18}} \cdot \frac{1}{T_s (\text{K})} \cdot \frac{1}{\Delta V_{\text{HI}} (\text{km s}^{-1})}, \quad (4)$$

where ΔV_{HI} , the HI linewidth, is given by $W_{\text{HI}}(\text{main})/(\text{peak HI brightness temperature})$, and T_{bg} is the background continuum radiation temperature (see Section 2.4.) including the 2.7 K cosmic background radiation (Fixsen 2009). $\tau_{\text{HI}}(\text{main})$ is the HI optical depth averaged over the HI velocity width ΔV_{HI} , which ranges from 8 km s^{-1} to 30 km s^{-1} with a median at $\sim 14 \text{ km s}^{-1}$. Note that equation (4) is valid not only for small τ_{HI} but also for any positive value of τ_{HI} . Figure 6 shows the two relationships in the T_s - $\tau_{\text{HI}}(\text{main})$ plane for four typical values of $T_s \simeq 20 \text{ K}$ (a), 40 K (b), 60 K (c), and 80 K (d). We estimate the errors in T_s as shown in Figure 6 from the 1σ noise level of the HI and $\tau_{353}(\text{main})$ data. We find that the equations give reasonable solutions with small errors for lower T_s , whereas

they cannot give a single set of T_s and $\tau_{\text{HI}}(\text{main})$ for T_s higher than ~ 70 K, where the error bars in T_s become uncomfortably large. In Figure 6, we estimate the error ranges as follows: (a) $T_s \simeq 20_{-2}^{+4}$ K, $\tau_{\text{HI}}(\text{main}) \simeq 1.06_{-0.29}^{+0.28}$, (b) $T_s \simeq 40_{-6}^{+13}$ K, $\tau_{\text{HI}}(\text{main}) \simeq 0.84_{-0.29}^{+0.28}$, (c) $T_s \simeq 60_{-20}^{+126}$ K, $\tau_{\text{HI}}(\text{main}) \simeq 0.31_{-0.22}^{+0.21}$, and (d) $T_s \simeq 80_{-39}^{+\infty}$ K, $\tau_{\text{HI}}(\text{main}) \simeq 0.16_{-0.16}^{+0.20}$. In the optically thin limit, the two equations become essentially the same, and can be satisfied by an infinite number of solutions, either a combination of large T_s and small $\tau_{\text{HI}}(\text{main})$, or that of small T_s and large $\tau_{\text{HI}}(\text{main})$. Only the lower limit for T_s and the upper limit of $\tau_{\text{HI}}(\text{main})$ are constrained.

Figure 7(a) shows the distribution of T_s , Figure 7(b) the distribution for $\tau_{\text{HI}}(\text{main})$, and Figure 7(c) the distribution of $\tau_{353}(\text{main})$. Several specific areas are masked as described in Section 3 and also masked where the estimated T_s is greater than 70 K. In Figure 7(a) T_s is mostly lower than 50 K. We also find that $\tau_{\text{HI}}(\text{main})$ becomes large in many of the data points. The results for T_s and $\tau_{\text{HI}}(\text{main})$ estimated are plotted in Figure 8 with superposition of equation (3) for T_s from 10 K to 100 K with $\tau_{\text{HI}}(\text{main})$. We see saturation of $W_{\text{HI}}(\text{main})$ becomes important for lower T_s , and the slope for a given T_s decreases with decreasing T_s due to saturation. This result is consistent with T_s estimated from comparisons between HI emission and absorption toward radio continuum sources, which show that cold HI clouds of 20 K–40 K are common (Dickey et al. 2003; Heiles & Troland 2003). Their spatial coverage is however much smaller than the present coverage, 100 square-degrees. Possible hints of optically thick HI are also found in the literature (Strasser & Taylor 2004; Dickey 2010).

5. Physical conditions in the HI gas

5.1. T_d and T_s

The present analysis offers evidence for a significant fraction of cold HI gas in the region. The analysis shows the typical physical parameters of the optically thick HI gas as follows: $N_{\text{HI}}(\text{main}) = 4 \times 10^{20} \text{ cm}^{-2}$ – $1.5 \times 10^{21} \text{ cm}^{-2}$, HI number density $n_{\text{HI}} = 40 \text{ cm}^{-3}$ – 160 cm^{-3} for cloud line-of-sight depth of 3 pc, and $T_s = 20 \text{ K}$ – 40 K . The gas kinetic temperature of the HI is determined by heating due to the interstellar radiation field (ISRF) and cooling mainly by the C II line (e.g., Wolfire et al. 1995) and is in a range from 10 K–100 K for column density higher than $2 \times 10^{20} \text{ cm}^{-2}$ (e.g., Goldsmith et al. 2007). Since the radiative transition rate, the Einstein A coefficient, of the 21 cm line is small, $\sim 3 \times 10^{-15} \text{ s}^{-1}$, the 21 cm transition is well thermalized by collisional excitation for density higher than $\sim 10 \text{ cm}^{-3}$ (e.g., Liszt 2001; Sato & Fukui 1978). T_s is exactly in equilibrium with the gas kinetic temperature in the dense HI gas. On the other hand, T_d is determined by the balance between the ISRF heating and thermal radiation of dust grains and is generally in a range from 15 K to 25 K in

the HI gas. T_d and T_s should show correlation, since heating is commonly due to the ISRF, where T_d variation is much smaller than that of T_s due to the strong temperature dependence of the dust cooling, as $(T_d)^6$ (e.g., Draine 2011). For A_V more than 1 mag, T_s becomes less than 60 K (e.g., Goldsmith et al. 2007), and T_d shows significant decrease to 17 K, which corresponds to T_d within the CO clouds (Figure 1). The present results on T_s and $\tau_{\text{HI}}(\text{main})$ are therefore consistent with the thermal properties of the ISM. It is possible that T_d is affected by the local radiation field in addition to the general ISRF. The distribution of T_d shown in Figure 1(c) indicates that in the northwest of the CO clouds T_d tends to be higher than in the southeast. This may be due to the excess radiation field of the OB stars in the Sco OB2 association which are located 100–200 pc away from the present clouds (c.f., Tachihara et al. 2001).

An X_{CO} factor converting W_{CO} into N_{H_2} is estimated from a comparison of CO and $\tau_{353}(\text{main})$ (Figure 5(b)). A least-squares fit for W_{CO} greater than 3.4 K km s^{-1} (above the 3σ noise level) yields $\tau_{353}(\text{main}) = [(1.8 \pm 0.8) \times 10^{-6}] \cdot W_{\text{CO}} (\text{K km s}^{-1}) + [(8.4 \pm 5.0) \times 10^{-6}]$. Here we adopt W_{CO} greater than 3σ by considering that an X_{CO} factor is conventionally estimated for $A_V \gtrsim 2\text{--}3$ mag (e.g. Bell et al. 2006). The offset 8.4×10^{-6} in $\tau_{353}(\text{main})$ in the above relationship is interpolated as due to the contribution of the HI, and the X_{CO} factor is calculated from the slope 1.8×10^{-6} in the relationship and the coefficient in equation (2) as $X_{\text{CO}} = N_{\text{H}_2}/W_{\text{CO}} = (1.5 \times 10^{26}/2) \cdot (1.8 \times 10^{-6}) = 1.3 \times 10^{20} \text{ cm}^{-2}/(\text{K km s}^{-1})$ with typical dispersion of $\sim \pm 40\%$, which is somewhat smaller than that estimated elsewhere, $(2\text{--}3) \times 10^{20} \text{ cm}^{-2}/(\text{K km s}^{-1})$ (e.g., Bertsch et al. 1993). Numerical simulations suggest that the X_{CO} factor is relatively uniform in regions of high visual extinction where CO is intense (Inoue & Inutsuka 2012; Glover & Mac Low 2011; Bell et al. 2006). This difference may be possibly ascribed to the large contribution of cold HI gas which was not taken into account previously, and should be confirmed by a careful analysis of more sample clouds. We note that we see a small number of points in Figure 5(b) which show higher $\tau_{353}(\text{main})$ for a given W_{CO} on the right of the dotted line and above the dashed line. These may correspond to the molecular gas with slightly less CO abundance than the majority, suggesting a younger chemical evolutionary stage (Yamamoto et al. 2003), and can be characterized by a higher X_{CO} factor.

5.2. Alternative ideas

The above interpretation assumes that all the neutral gas outside the CO is purely atomic. This interpretation is consistent with the present analysis including only HI as shown by the fit of the line radiation transfer equation and estimated T_s and $\tau_{\text{HI}}(\text{main})$

(Figure 7). We shall test if an interpretation based on CO-free H_2 is possible as an alternative, which was advocated for a giant molecular cloud having total mass of $10^5 M_\odot$ – $10^6 M_\odot$ by Wolfire et al. (2010) and was discussed in the first *Planck* paper (*Planck* Collaboration et al. 2011b). $\tau_{353}(\text{main})$ is a sum of the dust opacity both in the HI and H_2 gas. If CO-free H_2 is dominant, H_2 may account for most of the $\tau_{353}(\text{main})$ instead of HI. The observed value of $W_{\text{HI}}(\text{main})$ poses a strict lower limit on $N_{\text{HI}}(\text{main})$ and it is not probable that H_2 dominates HI. The majority of the data points have $T_s \sim 30$ K (Figure 8) and a lower limit for their HI column density is given by the optically thin limit. For instance, for points having $W_{\text{HI}}(\text{main}) = 250 \text{ K km s}^{-1}$, $N_{\text{HI}}(\text{main})$ at $T_s \sim 30$ K is $0.85 \times 10^{21} \text{ cm}^{-2}$, whereas $N_{\text{HI}}(\text{main})$ in the optically thin limit is $0.45 \times 10^{21} \text{ cm}^{-2}$ corresponding to $\sim 50\%$ of $0.85 \times 10^{21} \text{ cm}^{-2}$, and for points having $W_{\text{HI}}(\text{main}) = 200 \text{ K km s}^{-1}$, $N_{\text{HI}}(\text{main})$ at $T_s \sim 30$ K is $0.6 \times 10^{21} \text{ cm}^{-2}$ whereas $N_{\text{HI}}(\text{main})$ in the optically thin limit is $0.35 \times 10^{21} \text{ cm}^{-2}$ corresponding to $\sim 60\%$ of $0.6 \times 10^{21} \text{ cm}^{-2}$. This suggests that the cold gas typically has H_2 abundance of 50 % or less over most of the region outside of the CO clouds. Direct UV absorption measurements of H_2 abundances on the line of sight toward NGC 7469 ($\ell = 83^\circ 10, b = -45^\circ 47$) show $N_{\text{H}_2} = 4.7 \times 10^{19} \text{ cm}^{-2}$ and $N_{\text{HI}} = 3.9 \times 10^{20} \text{ cm}^{-2}$ (Gillmon et al. 2006), indicating that the hydrogen is about 90 % atomic. It is worth noting that other lines of sight at intermediate latitudes observed by *FUSE* and *Copernicus* (summarized by Rachford et al. 2009) show similarly low molecular fractions unless the total H column density, $N_{\text{H}_2} + N_{\text{HI}} \gtrsim 10^{21} \text{ cm}^{-2}$, lending support for the conclusion that HI is dominant. Finally, we note that the timescale for H_2 formation is generally as long as 10^7 years for typical density 100 cm^{-3} (Hollenbach et al. 1971). The cloud lifetime is however smaller than $\sim 10^6$ years as estimated from the crossing time at latitude higher than 10 degrees for a typical cloud size of several pc and a line width of 15 km s^{-1} (Yamamoto et al. 2003, 2006). This suggests that the present cloud is too young to form significant H_2 . Another possibility is that the dust properties may be considerably different in the region, as has been explored by the *Planck* collaboration (Planck Collaboration et al. 2014). We shall defer exploration of this possibility until a full account of the study is opened to the community.

5.3. Mass of the HI envelope

We estimate the total mass of the clouds in the region under study. We estimate the total system mass including HI, H_2 , and He (40 % of hydrogen in mass) to be $\sim 1.3 \times 10^4 M_\odot$, by using the sum of $\tau_{353}(\text{main})$ above 5×10^{-6} under equation (2) applied both to HI and H_2 (Figure 7(c)). The typical ratio of the opacity-corrected case to the optically thin case is estimated to be ~ 2.7 toward areas without CO emission, showing that the opacity correction has a significant impact. The mass of the HI gas in the masked areas is interpolated to be

$\sim 9.0 \times 10^2 M_\odot$ by using the average $N_{\text{HI}}(\text{main}) \sim 1.3 \times 10^{21} \text{ cm}^{-2}$ in the areas without masking, and corresponds to $\sim 7\%$ of the total system mass above. On the other hand, the molecular mass is estimated to be $\sim 1.2 \times 10^3 M_\odot$ by applying the present X_{CO} factor ($= 1.3 \times 10^{20} \text{ cm}^{-2}/(\text{K km s}^{-1})$) to the CO emission. Here we integrated the CO emission above the 3σ noise fluctuations of 3.4 K km s^{-1} in the integrated intensity in the 5 arcmin smoothed beam. By subtracting this mass from the total system mass, we obtain $\sim 1.2 \times 10^4 M_\odot$ as the total mass of the HI envelope. We thus find that the HI envelope has a total mass ~ 10 times larger than the mass of the H_2 clouds probed by CO. Note that in Gir et al. (1994) the mass of the HI envelope was calculated as $\sim 3 \times 10^3 M_\odot$, which is smaller than the present result. This difference may be attributed to the fact that (i) the area they used for the calculation corresponds to $\sim 1/2$ of that used in our calculation, and (ii) they assumed that all the HI gas is optically thin.

We conclude that the H_2 clouds traced by CO are surrounded by massive, optically thick HI envelopes possibly containing a relatively small fraction of H_2 that has no corresponding CO emission above the 3σ noise fluctuations of 3.4 K km s^{-1} . Figure 9 is a histogram of the mass of the HI envelope as a function of T_s . This clearly shows that most of the HI is in the T_s ranges from 20 K to 40 K. Assuming the depth of the HI envelope along the line of sight to be 3 pc, the HI density is estimated to be 40 cm^{-3} – 160 cm^{-3} . This density is consistent with $T_s = 20 \text{ K}$ – 40 K in a model calculation of the thermal balance (Goldsmith et al. 2007).

It is generally known that small clouds having mass less than $\sim 1000 M_\odot$ cannot be gravitationally bound due to the large virial mass as compared with the CO luminosity mass (e.g., Yonekura et al. 1997; Kawamura et al. 1998). The HI envelope may have a deep influence on cloud dynamics. The average density of the HI is 100 cm^{-3} and the velocity width is 15 km s^{-1} . The dynamical pressure of HI, ρv^2 [(density) \cdot (velocity dispersion) 2], is nearly equal to that of the H_2 gas and the pressure exerted by the HI envelope is able to confine the H_2 . The HI envelope may help to stabilize small H_2 clouds. It is yet perhaps true that the whole system including the HI envelope is not gravitationally bound because of the large velocity dispersion of the HI, and some dynamically transient states, like those in colliding HI flows, must be invoked to explain the cloud dynamics (e.g., Hartmann et al. 2001).

5.4. Relation to the dark gas

Recent analyses of gamma ray maps and the *Planck* data show evidence for dark gas which is not seen in CO or HI emission (Grenier et al. 2005; *Planck* Collaboration et al. 2011b). These analyses did not consider the HI opacity effect and assumed that HI is

completely optically thin. The present study has shown that the HI optical depth effect is important in this region and an upward correction of the cloud mass by a factor of ~ 2 on average is required. A significant fraction of the relatively dense HI gas may therefore be masked by saturation of the 21 cm line, and the cold HI gas is a viable candidate for the dark gas. This possibility deserves further exploration by including a much larger fraction of the sky. We note that the present analysis is applicable in a $\tau_{353}(\text{main})$ range from 2×10^{-6} to a few $\times 10^{-5}$. Therefore, the behavior of the HI outside this range is yet to be explored separately.

6. Conclusions

We have made a comparison of HI, CO, and the *Planck* dust properties in a complex of high latitude clouds MBM 53, 54, 55 and HLCG 92–35 and conclude from this study as follows;

The HI intensity shows a poor correlation with dust opacity with a correlation coefficient of ~ 0.6 . We interpret that this is caused by the effect of the optical depth on 21 cm HI emission. We present a method to estimate the spin temperature and the optical depth of the HI emission which couples the equation of line radiation transfer and the expression for the HI optical depth by assuming that dust properties do not change significantly in the region, where the $\tau_{353}(\text{main})$ is limited in a range from 3×10^{-6} to 2×10^{-5} . We have analyzed about 8×10^5 data points smoothed at 5 arcmin resolution and successfully estimated T_s and $\tau_{\text{HI}}(\text{main})$. Most of the points have T_s in the range from 20 K to 40 K and $\tau_{\text{HI}}(\text{main})$ is in the range from 0.2 to 4. This indicates that saturation due to large HI optical depth provides a reasonable explanation of the suppressed HI intensity in regions with large dust opacity. The T_s distribution is consistent with previous results estimated from absorption measurements toward radio continuum sources while in this paper the spatial coverage is continuous, covering a much larger area than continuum source absorption measurements. If the present results are correct, this suggests that optically thick HI is more significant than previously assumed in the literature. The typical physical parameters of the cold HI are density 40 cm^{-3} – 160 cm^{-3} , $T_s = 20 \text{ K}$ – 40 K and $N_{\text{HI}}(\text{main}) = 4 \times 10^{20} \text{ cm}^{-2}$ – $1.5 \times 10^{21} \text{ cm}^{-2}$. The X_{CO} factor to covert W_{CO} into N_{H_2} has been estimated to be $1.3 \times 10^{20} \text{ cm}^{-2} / (\text{K km s}^{-1})$. The CO clouds are associated with massive dense cold HI envelope having $\sim 1.2 \times 10^4 M_\odot$ as compared with the CO cloud mass of $\sim 1.2 \times 10^3 M_\odot$. Another possibility, that the dust properties may vary significantly, is being explored currently by the *Planck* collaboration, and should be considered in depth as a future step. Finally, it is an obvious task to extend this method to the whole sky to see if cold HI is common and dominant in the local interstellar

space around the Sun.

We are grateful to François Boulanger and Jean-Phillippe Bernard for their initiative to begin collaboration between the *Planck* and NANTEN2. The high latitude clouds in the paper were chosen as one of the primary targets in the comparative study. We thank the anonymous referee for the valuable comments on the paper.

NANTEN2 is an international collaboration among 10 universities; Nagoya University, Osaka Prefecture University, University of Cologne, University of Bonn, Seoul National University, University of Chile, University of New South Wales, Macquarie University, University of Sydney, and University of ETH Zurich. This work was financially supported by Grants-in-Aid for Scientific Research (KAKENHI) of Japanese society for the Promotion of Science (JSPS) (grant numbers 24224005, 25287035, 23403001, 23540277, and 23740149-01). This work was also financially supported by the Young Research Overseas Visits Program for Vitalizing Brain Circulation (R2211) and the Institutional Program for Young Researcher Overseas Visits (R29) by the Japan Society for the Promotion of Science (JSPS) and by the grant-in-aid for Nagoya University Global COE Program, “Quest for Fundamental Principles in the Universe: From Particles to the Solar System and the Cosmos,” from MEXT. Based on observations obtained with *Planck* (<http://www.esa.int/Planck>), an ESA science mission with instruments and contributions directly funded by ESA Member States, NASA, and Canada. This publication utilizes data from Galactic ALFA HI (GALFA HI) survey data set obtained with the Arecibo L-band Feed Array (ALFA) on the Arecibo 305 m telescope. Arecibo Observatory is part of the National Astronomy and Ionosphere Center, which is operated by Cornell University under Cooperative Agreement with the U.S. National Science Foundation. The GALFA HI surveys are funded by the NSF through grants to Columbia University, the University of Wisconsin, and the University of California. Some of the results in this paper have been estimated using the HEALPIX (Górski et al. 2005) package.

Appendix A

Figure 10 shows five HI velocity channel distributions from $V_{\text{LSR}} = -45 \text{ km s}^{-1}$ to $+32 \text{ km s}^{-1}$. The main HI cloud toward the CO emitting clouds is seen from -12.7 km s^{-1} to -0.3 km s^{-1} (panel (b)) as noted by Gir et al. (1994). The main feature is outstanding in the HI intensity having 200 K km s^{-1} in the integrated intensity. In this velocity channel, we see additional HI features; one is located ~ 5 degree west of the main cloud and is elongated in a similar direction and with similar length to the main cloud (called West1 HI), and the other in the north of the main cloud peaked at $(l, b) \sim (100^\circ, -31^\circ)$ (North HI). West1 HI

seems to be linked with the northern tip of the CO clouds. We also find an additional feature (West2 HI) peaked at $(l, b) \sim (90^\circ, -37^\circ)$ which may be extended to the west up to $l \sim 80^\circ$.

In V_{LSR} from -25.0 km s^{-1} to -12.7 km s^{-1} (panel (a)), we see two features; one of them corresponds to North HI in position and the other to West2 HI. In addition, the HI, North HI and several smaller peaks along the southern rim of the main cloud, seems to be surrounding the CO as noted by Yamamoto et al. (2003) (see also their Figure 6).

In the velocity from -0.3 km s^{-1} to $+12.0 \text{ km s}^{-1}$ (panel (c)), we see the HI corresponds to West1 HI and the HI in the north shows intensity depression surrounding the CO, suggesting physical association with the CO.

In the other extreme velocity range from -45.0 km s^{-1} to -25.0 km s^{-1} (panel (d)) we find the main peak at $(l, b) \sim (87^\circ, -38^\circ)$ shows elongation similar to West2 HI. The HI may be possibly linked with West2, while it was not included in the present analysis.

We summarize the above that the HI in the three panels (a), (b) and (c) is likely associated with the main cloud within a volume having a size in the order of the main HI cloud, 30–40 pc, at a distance of 150 pc.

Appendix B

$\tau_{353}(\text{main})$, which is the main component of τ_{353} , is calculated as follows;

- (1) First we use slope derived by least-squares fits between W_{HI} and τ_{353} by linear regression for $T_d > 21.5 \text{ K}$ in Figure 4(b).
- (2) By using the slope derived from (1) τ'_{353} is calculated by $\tau'_{353} = \tau_{353} - W_{\text{HI}} (V_{\text{LSR}} < -25 \text{ km s}^{-1}, +12 \text{ km s}^{-1} < V_{\text{LSR}}) / (\text{slope})$.
- (3) We estimate new slope again by the same manner as (1) between $W_{\text{HI}}(\text{main})$ and τ'_{353} .
- (4) τ''_{353} is calculated by the same manner as (2) but by using τ'_{353} and the slope derived by (3).
- (5) Iterating (3) and (4) until the value of the slope becomes converged.

After 5 iterations the best estimate of the slope k converged to $8.34 \times 10^7 \text{ K km s}^{-1}$ with the relative variation less than 10^{-4} .

REFERENCES

- Abdo, A. A., Ackermann, M., Ajello, M., et al. 2011, *ApJ*, 733, L26
- Bell, T. A., Roueff, E., Viti, S., & Williams, D. A. 2006, *MNRAS*, 371, 1865
- Bertsch, D. L., Dame, T. M., Fichtel, C. E., et al. 1993, *ApJ*, 416, 587
- Blitz, L., Fukui, Y., Kawamura, A., et al. 2007, *Protostars and Planets V*, 81
- Bolatto, A. D., Wolfire, M., & Leroy, A. K. 2013, *ARA&A*, 51, 207
- Calabretta, M. R., Staveley-Smith, L., & Barnes, D. G. 2014, *PASA*, 31, 7
- Castets, A., Duvert, G., Dutrey, A., et al. 1990, *A&A*, 234, 469
- Dickey, J. M. 2010, *Planets, stars and stellar systems.*, Vol. 5: Galactic Structure and Stellar Populations (Berlin: Springer)
- Dickey, J. M., & Lockman, F. J. 1990, *ARA&A*, 28, 215
- Dickey, J. M., McClure-Griffiths, N. M., Gaensler, B. M., & Green, A. J. 2003, *ApJ*, 585, 801
- Draine, B. T. 2011, *Physics of the Interstellar and Intergalactic Medium* (Princeton, NJ: Princeton Univ. Press)
- Emerson, D. T., & Graeve, R. 1988, *A&A*, 190, 353
- Fixsen, D. J. 2009, *ApJ*, 707, 916
- Fukuda, T., Yoshiike, S., Sano, H., et al. 2014, *ApJ*, 788, 94
- Fukui, Y. 2013, in *Advances in Solid State Physics*, Vol. 34, *Cosmic Rays in Star-Forming Environments*, ed. D. F. Torres & O. Reimer (Berlin: Springer), 249
- Fukui, Y., & Kawamura, A. 2010, *ARA&A*, 48, 547
- Fukui, Y., Sano, H., Sato, J., et al. 2012, *ApJ*, 746, 82
- Fukui, Y., Torii, K., Onishi, T., et al. 2014, *ApJ* in press, arXiv:1403.0999v1
- Gillmon, K., Shull, J. M., Tumlinson, J., & Danforth, C. 2006, *ApJ*, 636, 891
- Gir, B.-Y., Blitz, L., & Magnani, L. 1994, *ApJ*, 434, 162

- Glover, S. C. O., & Mac Low, M.-M. 2011, MNRAS, 412, 337
- Goldsmith, P. F., Li, D., & Krčo, M. 2007, ApJ, 654, 273
- Górski, K. M., Hivon, E., Banday, A. J., et al. 2005, ApJ, 622, 759
- Grenier, I. A., Casandjian, J.-M., & Terrier, R. 2005, Science, 307, 1292
- Hartmann, L., Ballesteros-Paredes, J., & Bergin, E. A. 2001, ApJ, 562, 852
- Heiles, C., & Troland, T. H. 2003, ApJ, 586, 1067
- Hollenbach, D. J., Werner, M. W., & Salpeter, E. E. 1971, ApJ, 163, 165
- Ichiki, K., Kaji, R., Yamamoto, H., Takeuchi, T. T., & Fukui, Y. 2014, ApJ, 780, 13
- Inoue, T., & Inutsuka, S.-i. 2012, ApJ, 759, 35
- Kalberla, P. M. W., & Kerp, J. 2009, ARA&A, 47, 27
- Kawamura, A., Onishi, T., Yonekura, Y., et al. 1998, ApJS, 117, 387
- Lee, M.-Y., Stanimirović, S., Douglas, K. A., et al. 2012, ApJ, 748, 75
- Liszt, H. 2001, A&A, 371, 698
- Magnani, L., Blitz, L., & Mundy, L. 1985, ApJ, 295, 402
- Peek, J. E. G., Heiles, C., Douglas, K. A., et al. 2011, ApJS, 194, 20
- Planck Collaboration, Abergel, A., Ade, P. A. R., et al. 2014, A&A, 571, A11
- Planck* Collaboration, Abergel, A., Ade, P. A. R., et al. 2011a, A&A, 536, A24
- Planck* Collaboration, Ade, P. A. R., Aghanim, N., et al. 2011b, A&A, 536, A19
- . 2011c, A&A, 536, A23
- . 2011d, A&A, 536, A22
- Planck* Collaboration, Abergel, A., Ade, P. A. R., et al. 2011e, A&A, 536, A21
- . 2011f, A&A, 536, A25
- . 2014, A&A, 566, A55
- Rachford, B. L., Snow, T. P., Destree, J. D., et al. 2009, ApJS, 180, 125

- Reich, P., & Reich, W. 1986, A&AS, 63, 205
- Reich, W. 1982, A&AS, 48, 219
- Sato, F., & Fukui, Y. 1978, AJ, 83, 1607
- Strasser, S., & Taylor, A. R. 2004, ApJ, 603, 560
- Tachihara, K., Toyoda, S., Onishi, T., et al. 2001, PASJ, 53, 1081
- Planck* Collaboration. 2013, *Planck* Explanatory Supplement (Public Release 1) (Noordwijk: ESA)
- Welty, D. E., Hobbs, L. M., Penprase, B. E., & Blitz, L. 1989, ApJ, 346, 232
- Wolfire, M. G., Hollenbach, D., & McKee, C. F. 2010, ApJ, 716, 1191
- Wolfire, M. G., Hollenbach, D., McKee, C. F., Tielens, A. G. G. M., & Bakes, E. L. O. 1995, ApJ, 443, 152
- Yamamoto, H., Kawamura, A., Tachihara, K., et al. 2006, ApJ, 642, 307
- Yamamoto, H., Onishi, T., Mizuno, A., & Fukui, Y. 2003, ApJ, 592, 217
- Yonekura, Y., Dobashi, K., Mizuno, A., Ogawa, H., & Fukui, Y. 1997, ApJS, 110, 21

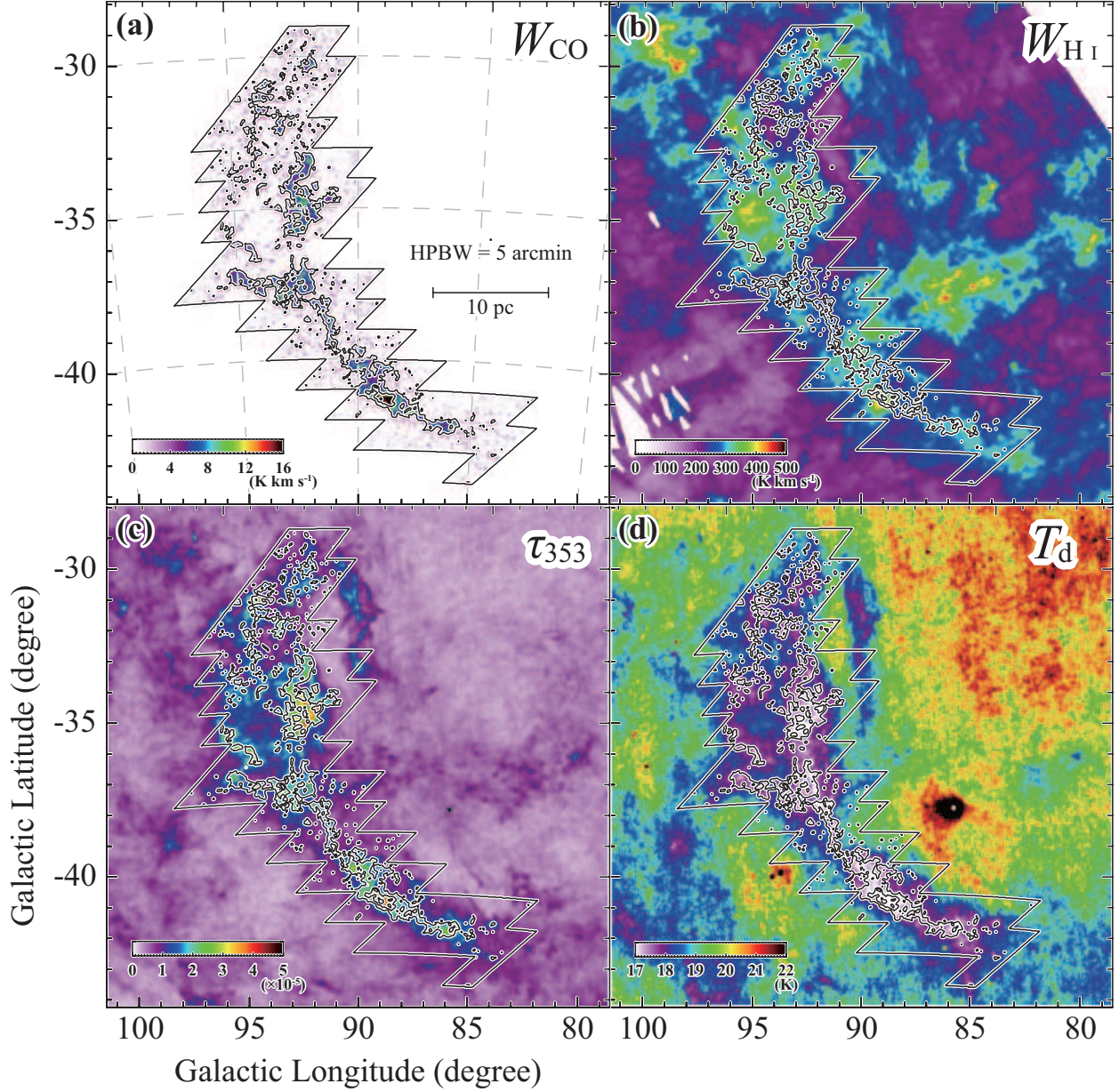


Fig. 1.— (a) Velocity-integrated intensity map of $^{12}\text{CO}(J=1-0)$ in the galactic coordinates. The integrated LSR-velocity range is from -12 km s^{-1} to $+2 \text{ km s}^{-1}$. The contours are drawn every 7.9 K km s^{-1} from 3.4 K km s^{-1} . The bounding box shows the observed area. (b), (c), and (d) are spatial distributions of velocity-integrated intensity of the HI (W_{HI}), the optical depth at 353 GHz (τ_{353}), and the temperature of the cold dust (T_d), respectively. The contours of CO and the bounding boxes are the same as in (a). The integrated velocity range of the W_{HI} in (b) is from -49 km s^{-1} to $+17 \text{ km s}^{-1}$. The effective beam sizes are 5 arcmin for the 4 panels.

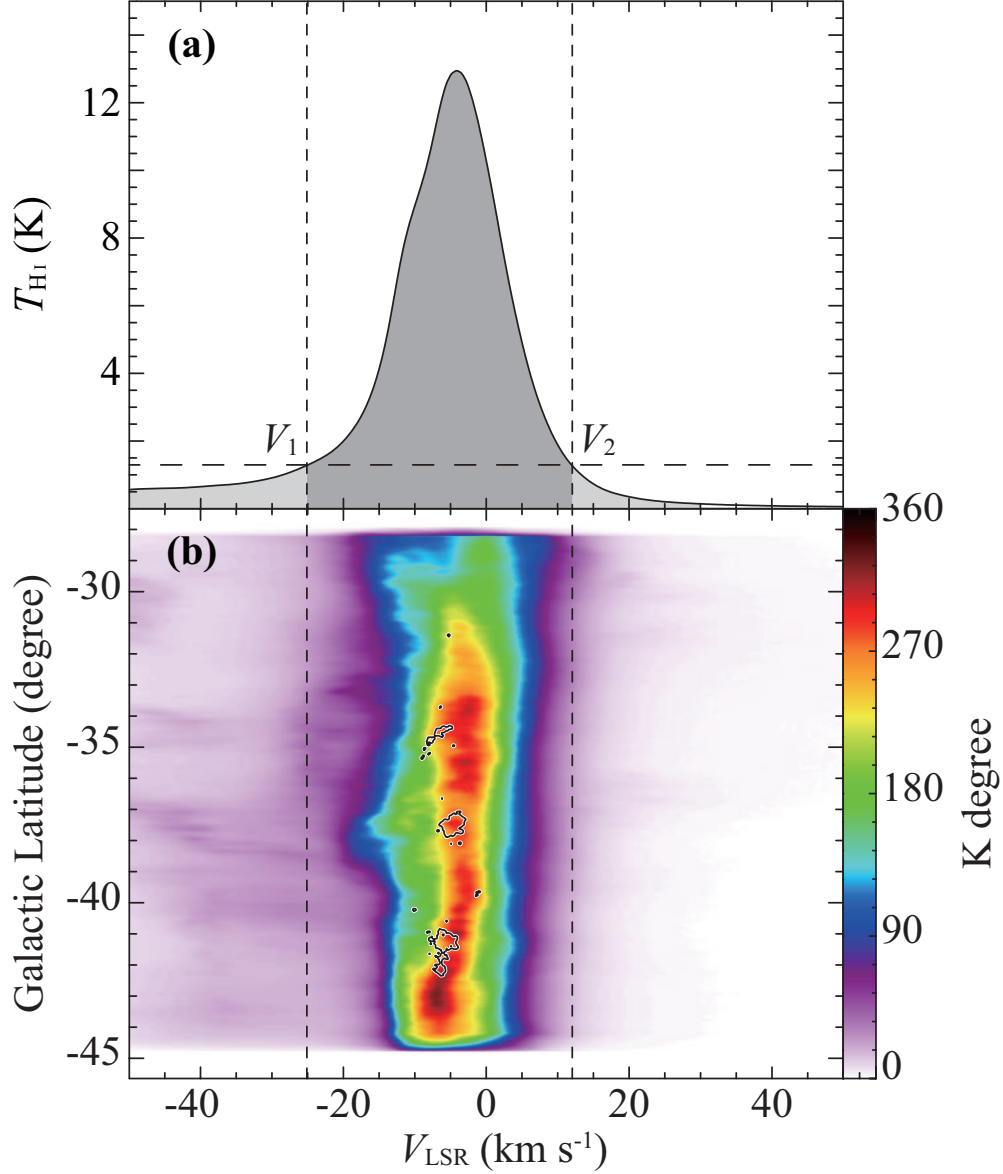


Fig. 2.— (a) Average spectrum of the HI in the region shown in Figure 1(d), but the masking described in Section 2.5. are applied. T_{mb} at $V_1 = -25 \text{ km s}^{-1}$ and at $V_2 = +12 \text{ km s}^{-1}$ correspond to 10 % level of the peak. (b) Latitude-velocity diagram of HI (color image) and CO (contours) integrated over the longitude range in Figure 1. The integrating range are from $\ell \sim 80^\circ$ to $\sim 100^\circ$. The level of the CO contours is $\sim 3 \text{ K degree}$. 89 % of the HI emission is concentrated in the velocity range from -25 km s^{-1} to $+12 \text{ km s}^{-1}$.

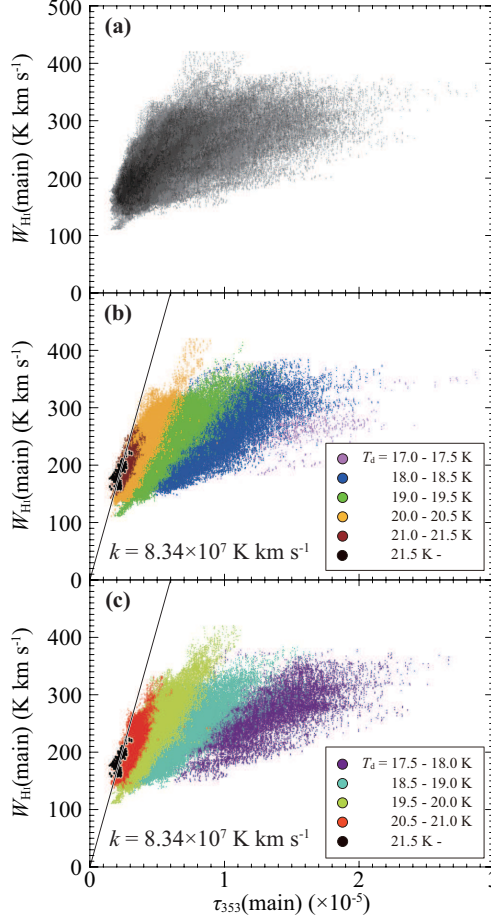


Fig. 3.— Scatter plots between $W_{\text{HI}}(\text{main})$ and $\tau_{353}(\text{main})$ and between W_{HI} and τ_{353} in the region shown in Figure 1. Specific areas are masked. Details on the masking are described in Section 2.5. **Figure 3:** scatter plots of $W_{\text{HI}}(\text{main})$ whose integrated velocity range is from -25 km s^{-1} to $+12 \text{ km s}^{-1}$ and $\tau_{353}(\text{main})$, which is the τ_{353} component associated with the HI whose velocity range is from -25 km s^{-1} to $+12 \text{ km s}^{-1}$. Details on how to calculate this $\tau_{353}(\text{main})$ value are described in the Appendix B. **(a)** plots in black dots for all points. **(b)** and **(c)** show the scatter plots for T_d in windows of 0.5 K interval every 1 K. In order to avoid heavy overlapping among the data points, in **(b)** we show five T_d ranges, 17.0 K–17.5 K (light purple), 18.0 K–18.5 K (blue), 19.0 K–19.5 K (green), 20.0 K–20.5 K (yellow), and 21.0 K–21.5 K (brown), and in **(c)** five T_d ranges shifted by 0.5 K, 17.5 K–18.0 K (purple), 18.5 K–19.0 K (light blue), 19.5 K–20.0 K (light green), and 20.5 K–21.0 K (red). In the both panels **(b)** and **(c)** the T_d range, 21.5 K and higher, is shown in black along with the linear regression line obtained by the least-squares fit which is assumed to have zero intercept. **Figure 4:** same as Figure 3 but integrated velocity range of the HI is from -49 km s^{-1} to $+17 \text{ km s}^{-1}$ and τ_{353} is the total value.

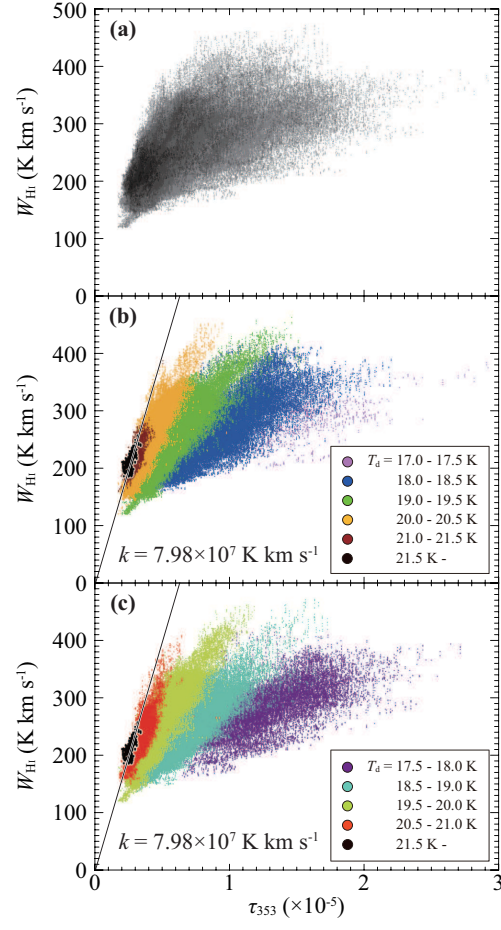


Fig. 4.—

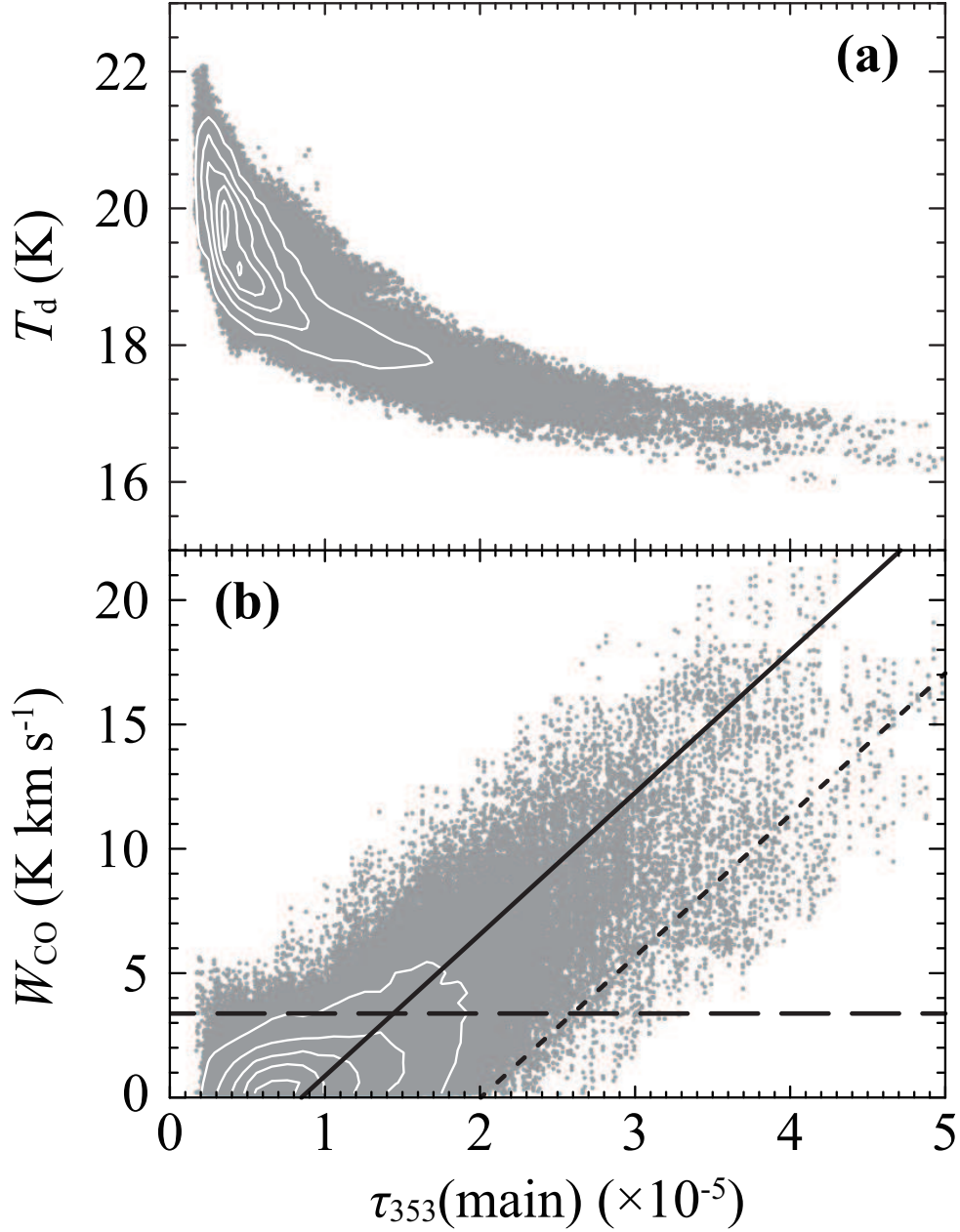


Fig. 5.— **(a)** Correlation plot between T_d and $\tau_{353}(\text{main})$ in the area shown in Figure 7(c). The contours represent the 90 %, 70 %, 50 %, 30 %, and 10 % levels of the maximum of the density of the plotted data over the $(T_d, \tau_{353}(\text{main}))$ space. **(b)** same as **(a)** but for W_{CO} and $\tau_{353}(\text{main})$. The contours represent the 90 %, 70 %, 50 %, 30 %, and 10 % levels of the maximum of the density of the plotted data over the $(W_{\text{CO}}, \tau_{353}(\text{main}))$ space. The dashed line represents 3σ level of the CO data (3.4 K km s^{-1}), and the solid line a relationship $\tau_{353}(\text{main}) = [(1.8 \pm 0.8) \times 10^{-6}] \cdot W_{\text{CO}} (\text{K km s}^{-1}) + [(8.4 \pm 5.0) \times 10^{-6}]$, which is the result of a least-squares fit to the data with $W_{\text{CO}} > 3\sigma$. The dotted line is $\tau_{353}(\text{main}) = (1.8 \times 10^{-6}) \cdot W_{\text{CO}} (\text{K km s}^{-1}) + (2 \times 10^{-5})$ (see text).

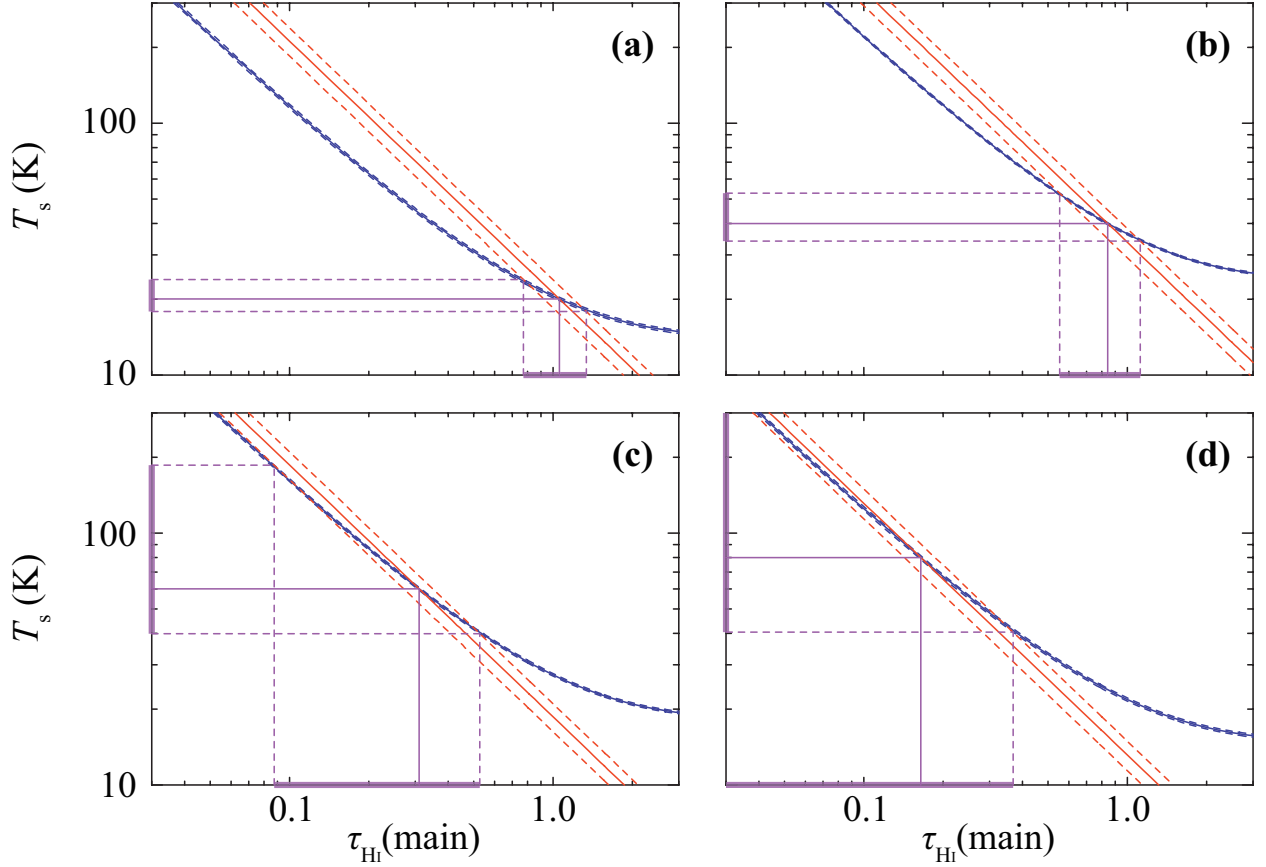


Fig. 6.— The blue and red lines represent equations (3) and (4) in the text, respectively. The crossing point of the two lines is the solution that satisfies both equations (3) and (4). (a), (b), (c), and (d) show the typical cases of the solutions of $T_s \simeq 20$ K, $\simeq 40$ K, $\simeq 60$ K, and $\simeq 80$ K, and are located at $(\ell, b) \sim (92^\circ 70, -41^\circ 56)$, $(90^\circ 07, -42^\circ 68)$, $(89^\circ 69, -29^\circ 12)$, and $(86^\circ 03, -30^\circ 09)$, respectively. The dashed lines around each line are the error taking observational parameters into consideration. The purple solid lines indicate the solutions of $\tau_{\text{HI}}(\text{main})$ and T_s , and dashed lines their errors.

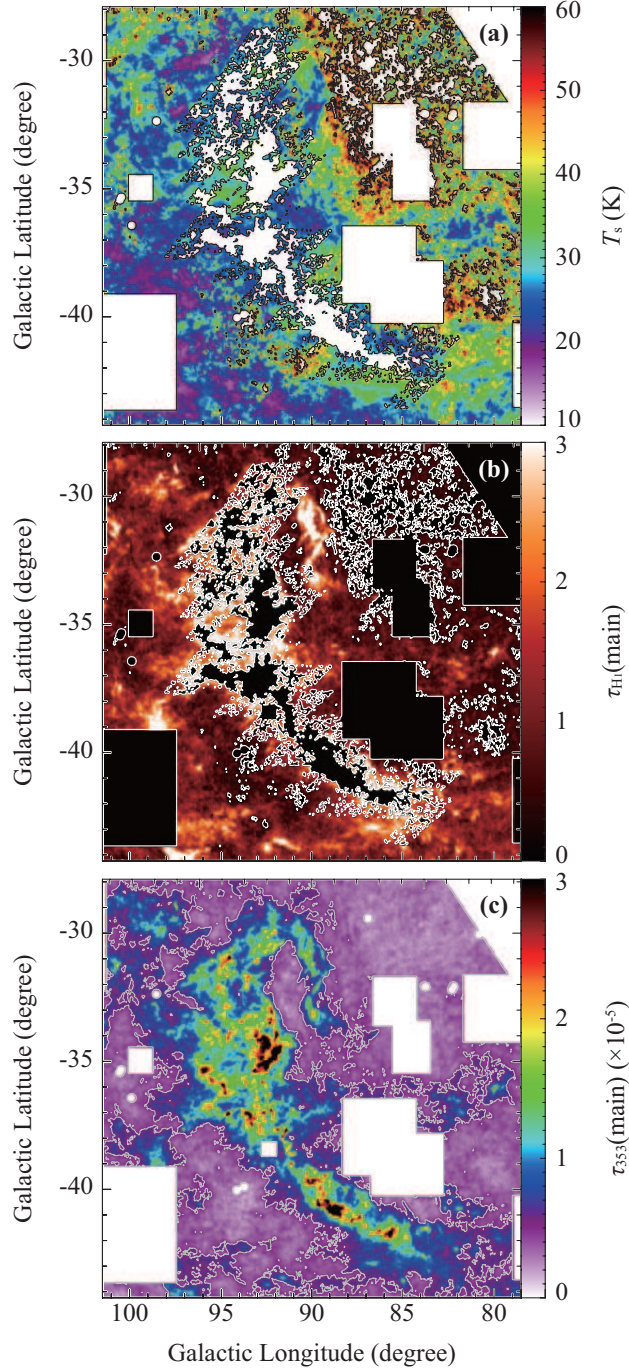


Fig. 7.— (a) and (b) show the spatial distribution of T_s and $\tau_{\text{H I}}(\text{main})$ solved from the two equations (3) and (4) in the text. The masks described in Section 2.5. are applied, and in addition the areas where $T_s \geq 70$ K are masked. (c) represents the spatial distribution of $\tau_{353}(\text{main})$. The gray contours indicate the level of $\tau_{353}(\text{main}) = 5 \times 10^{-6}$.

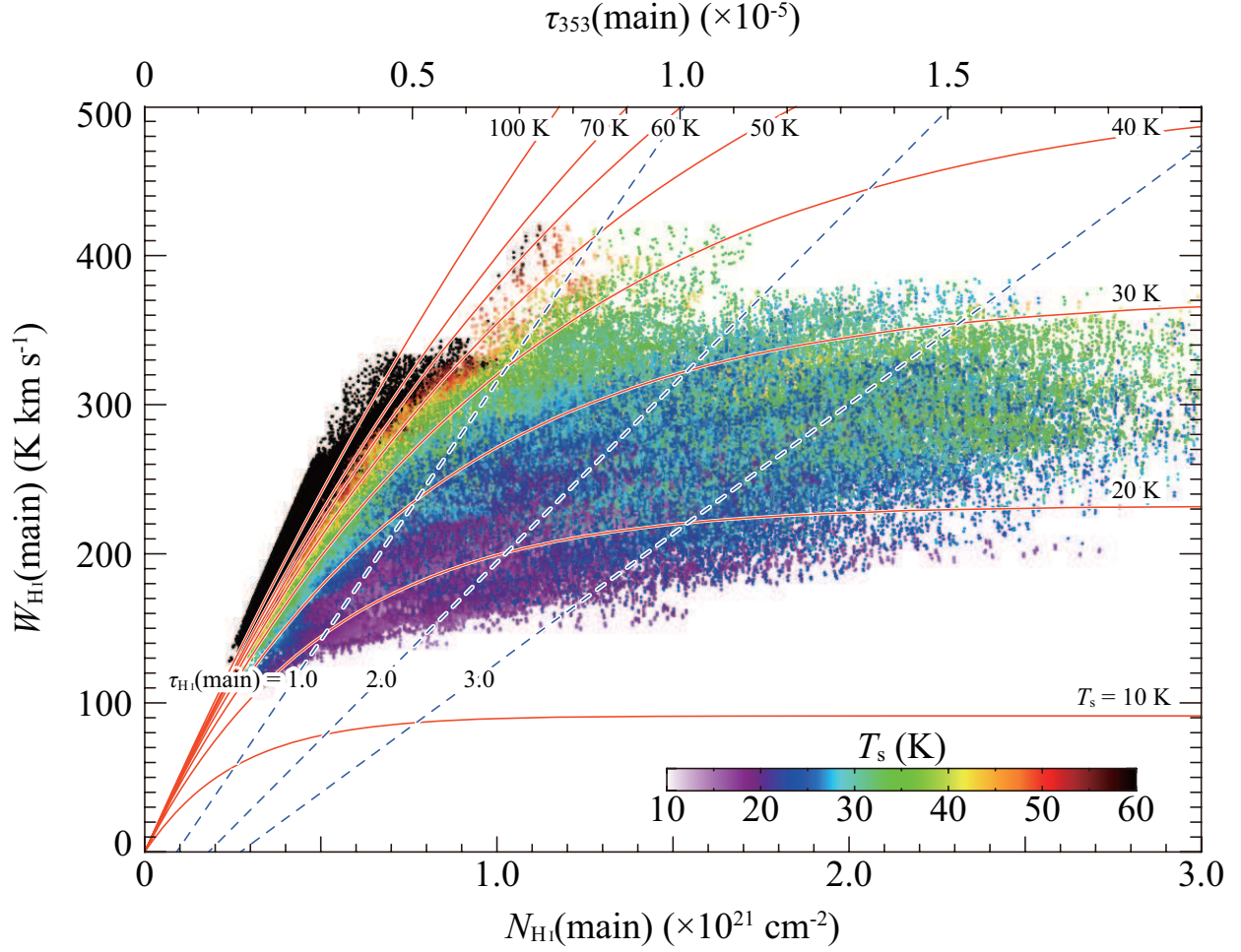


Fig. 8.— Correlation plot between $W_{\text{HI}}(\text{main})$ and $N_{\text{HI}}(\text{main})$. The data in the region shown in the Figure 7(a)(b) is plotted. The color of each point represents T_s . The solid and dashed lines represent T_s and $\tau_{\text{HI}}(\text{main})$ calculated from equations (3) and (4) in the text by assuming ΔV_{HI} of $\sim 14.1 \text{ km s}^{-1}$ (median value) and T_{bg} of $\sim 3.5 \text{ K}$ (median value), respectively.

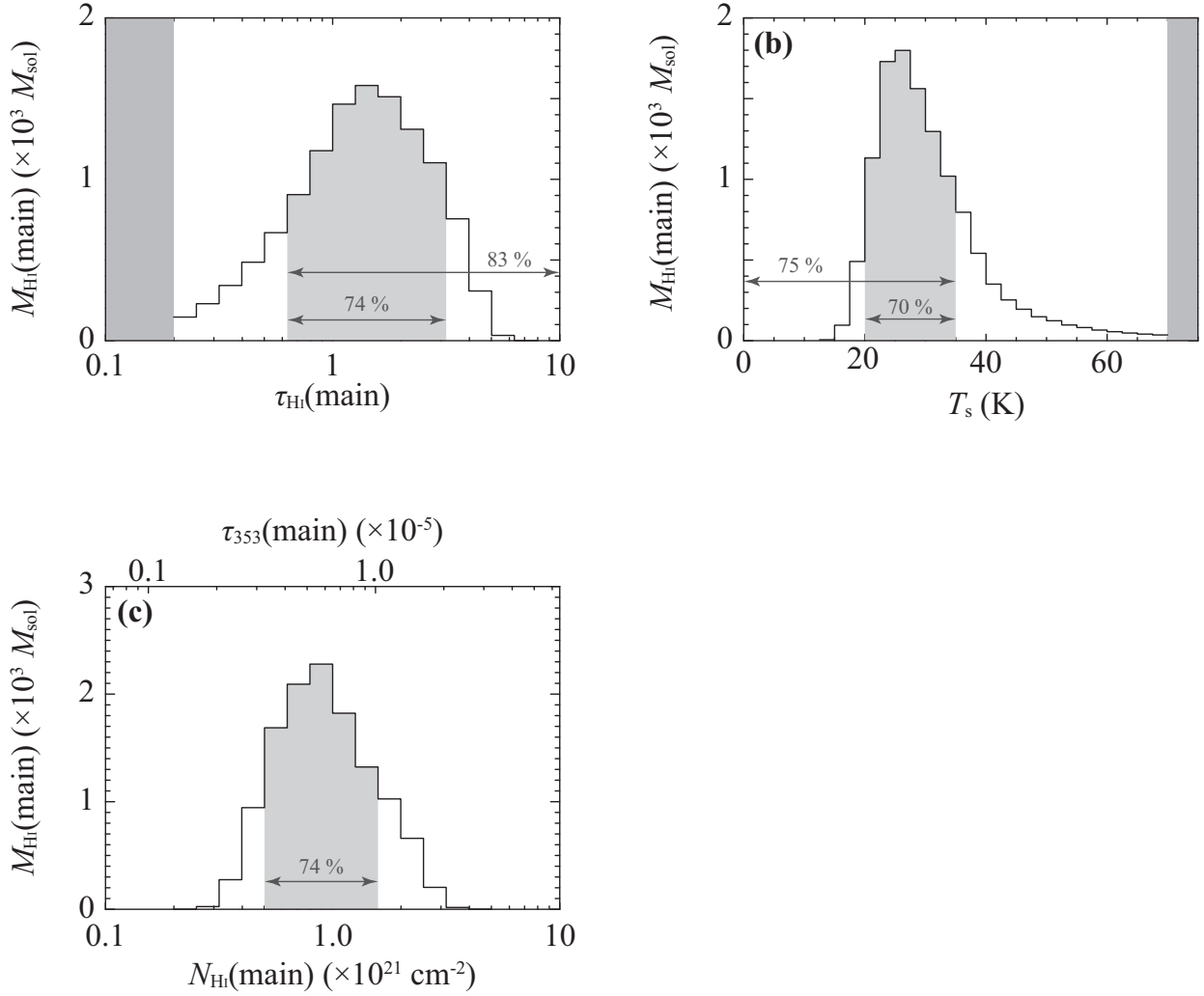


Fig. 9.— **(a)** Histogram of the mass of the HI envelope as a function of $\tau_{\text{HI}}(\text{main})$. **(b)** The same as **(a)**, but as a function of T_s . **(c)** The same as **(a)** and **(b)**, but as functions of $N_{\text{HI}}(\text{main})$ and $\tau_{353}(\text{main})$. The areas filled with light-gray are determined by the widths at the half-levels of the each histogram. Note that in panels (a) and (b), the histograms where $\tau_{\text{HI}}(\text{main}) \leq 0.2$ or $T_s \geq 70$ K are masked because the solutions of $\tau_{\text{HI}}(\text{main})$ and T_s are not well-estimated.

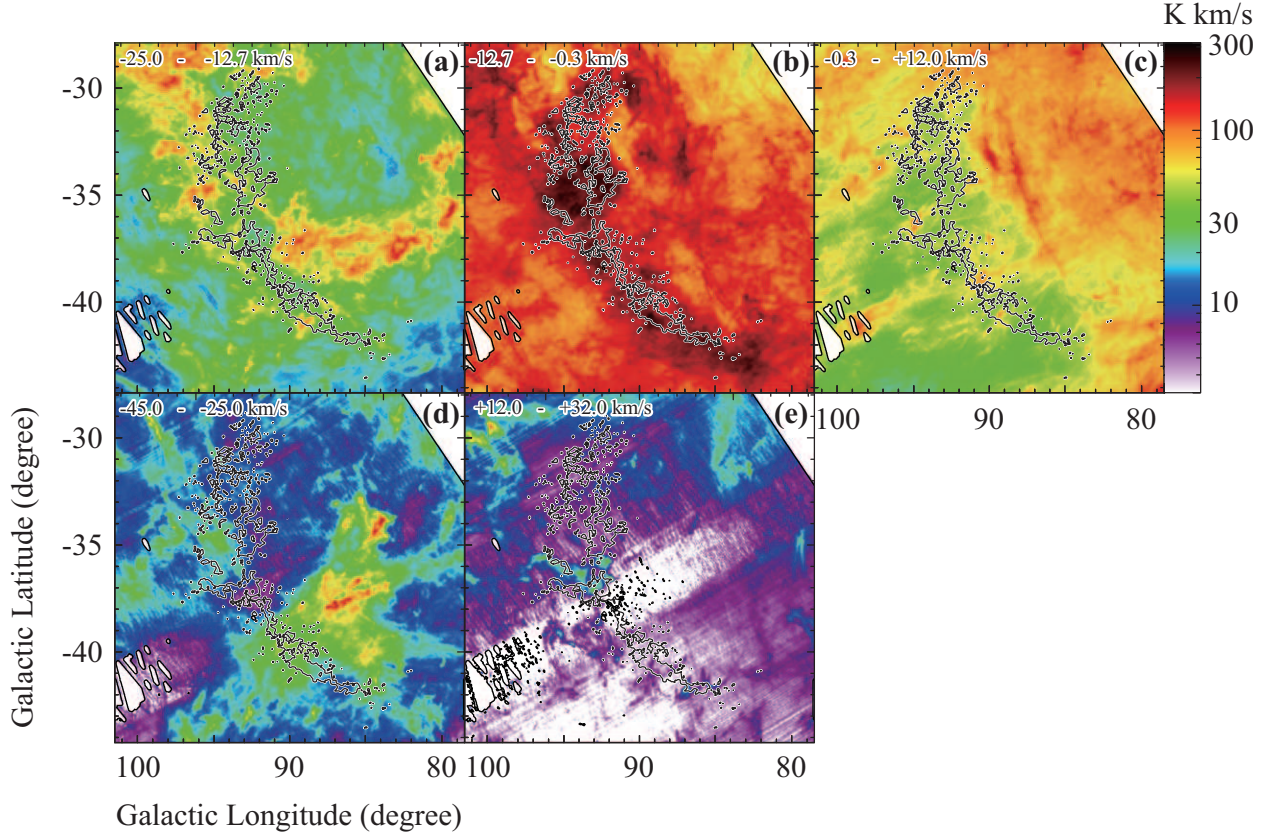


Fig. 10.— Velocity channel maps of the HI (color image) superposed on the W_{CO} (contours). In panels (a), (b), and (c), we show the channel maps of the main HI cloud with dividing the velocity range into three. Panels (d) and (e) show the channel maps outside the main HI velocity range. The contour level of W_{CO} is 3.4 K km s^{-1} for each panel.

Table 1. List of masked areas

position		Area	Object name	Remark
ℓ (degree)	b (degree)	(degree ²)		
79.1	−41.8	1.1	...	(a)
81.5	−29.3	6.5	...	(a)
81.5	−33.0	6.0	...	(b)
85.6	−33.8	6.4	...	(b)
86.1	−38.2	13.1	3C 454.3	(c)
92.2	−38.9	0.3	...	(a)
98.3	−35.1	1.0	...	(a)
99.1	−41.6	13.1	...	(a)
99.4	−30.1	0.7	...	(a)
80.58	−32.47	8.5×10^{-2}	IRAS 22221+1748	infrared source
82.42	−30.16	8.5×10^{-2}	33 Peg	double or multiple star
83.37	−32.25	8.6×10^{-2}	Mrk 306	galaxy
83.46	−32.39	8.6×10^{-2}	HD 213618	star
84.67	−32.34	8.7×10^{-2}	HD 214128	star
84.73	−32.31	8.7×10^{-2}	NGC 7316	galaxy
86.05	−33.18	8.6×10^{-2}	Mrk 308	Seyfert galaxy
86.09	−33.57	8.6×10^{-2}	BD+19 4992	star
87.46	−29.73	8.6×10^{-2}	NGC 7339	radio galaxy ^(d)
93.53	−40.35	8.7×10^{-2}	RAFGL 3068	variable star
93.91	−40.47	8.7×10^{-2}	NGC 7625	interacting galaxies
97.29	−32.52	8.6×10^{-2}	IC 5298	Seyfert 2 galaxy
98.88	−36.55	8.6×10^{-2}	NGC 7678	active galaxy nucleus
99.24	−35.40	8.6×10^{-2}	NGC 7673	emission-line galaxy
99.32	−35.49	8.6×10^{-2}	NGC 7677	galaxy in pair of galaxies

^(a)The HI data is missing.

^(b)There are secondary HI peaks outside the velocity range from -25 km s^{-1} to $+12 \text{ km s}^{-1}$.

^(c)Abdo et al. (2011)

^(d)While this object is not listed in the *IRAS* point source catalog, T_{d} is locally high around this object.

Note. — Columns 1 and 2 give the positions of each mask, and column 3 gives their areas. Column 4 indicates object names located at the center of each mask. Remarks on each masked area are listed in column 5. Details on these masked areas are described in Section 2.5.

Table 2. Parameters of the data points in each T_d range

T_d (K)	N_{pixel}	Slope k (K km s ⁻¹)	Intercept (K km s ⁻¹)	C.C.
17.0–17.5	1.48×10^3	6.83×10^6	1.5×10^2	0.62
17.5–18.0	2.73×10^4	9.85×10^6	1.4×10^2	0.72
18.0–18.5	8.64×10^4	1.41×10^7	1.2×10^2	0.80
18.5–19.0	1.53×10^5	1.92×10^7	1.1×10^2	0.81
19.0–19.5	1.61×10^5	2.50×10^7	0.96×10^2	0.86
19.5–20.0	1.42×10^5	3.24×10^7	0.88×10^2	0.88
20.0–20.5	9.52×10^4	4.03×10^7	0.77×10^2	0.86
20.5–21.0	4.33×10^4	4.08×10^7	0.81×10^2	0.79
21.0–21.5	1.13×10^4	3.54×10^7	1.0×10^2	0.71
≥ 21.5	7.18×10^2	8.34×10^7	...	0.62

Note. — N_{pixel} is the number of pixels in each T_d range. C.C. indicates the correlation coefficients for the points in each T_d range. Columns 3 and 4 give values of the slope and intercept of the best fit linear relationship between $W_{\text{HI}}(\text{main})$ and $\tau_{353}(\text{main})$ (Figure 3). The last row gives the slope assuming the intercept is zero in this case. The data are fitted by least-squares method.